Journal of Environmental Radioactivity 282 (2025) 107592

Contents lists available at ScienceDirect

Journal of Environmental Radioactivity

journal homepage: www.elsevier.com/locate/jenvrad

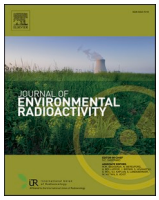

The impact of ENSO on near-surface Beryllium-7

K. Schaar [a,*], T. Spiegl [a,b], T. Sato [c], U. Langematz [a]

[a] Institut für Meteorologie, Freie Universität Berlin, Berlin, Germany
[b] Alfred-Wegener-Institut, Bremerhaven, Germany
[c] Japan Atomic Energy Agency, Tokai, Japan

A B S T R A C T

The concentration of near-surface Beryllium-7 contains valuable information about the atmosphere, e.g., the tropospheric circulation, precipitation pattern or specific atmospheric phenomena, like the El Niño Southern Oscillation. Here, we modelled the transport and deposition of Beryllium-7 from galactic cosmic rays for 1850–2100, using the ECHAM/MESSy atmospheric chemistry climate model, and analyzed the variability of near-surface Beryllium-7 due to the El Niño Southern Oscillation. We find that our simulated Beryllium-7 time series agree well with Beryllium-7 measurements from the international monitoring system of the Comprehensive Nuclear-Test-Ban Treaty Organization. The analysis of the time series reveals significant Beryllium-7 patterns for El Niño and La Niña in the equatorial Pacific region, controlled by precipitation anomalies and the respective state of the Walker Circulation. Furthermore, our simulations show an intensification of the Beryllium-7 pattern for El Niño and La Niña in the future. Additionally, our findings suggest that near-surface Beryllium-7 could be used as an additional indicator or even predictor of the upcoming phase of the El Niño Southern Oscillation.

1. Introduction

Cosmogenic Beryllium-7 (hereafter ^{7}Be) is a natural radionuclide with a half-life of 53.3 days. It is continuously produced in the lower stratosphere and upper troposphere as a result of spallation reactions of galactic cosmic rays (GCRs) with the nuclei of atmospheric gases, mainly oxygen and nitrogen (Terzi and Kalinowski, 2017). Furthermore, the production of ^{7}Be is modulated by the 11-year solar cycle because in phases of higher magnetic shielding by the Sun (during solar maximum) from GCR, less cosmogenic nuclides are produced in the atmosphere and vice versa (Lal and Peters, 1962; Beer et al., 1994; Usoskin, 2017). Typically, over 60% of cosmogenic ^{7}Be is produced in the stratosphere (Golubenko et al., 2022), where it attaches to stratospheric aerosols, e.g., sulfuric acid droplets from the Junge layer (Junge, 1963), shortly after the production. ^{7}Be produced in the troposphere attaches to tropospheric aerosols, such as water droplets, sea salt, dust, pollen or volcanic aerosols, which can be much larger than stratospheric aerosols (Pandis et al., 1995).

The transport of aerosols and thus also cosmogenic ^{7}Be in the stratosphere is mainly driven by the Brewer-Dobson Circulation (BDC), which describes the net transport of air mass in the middle atmosphere (for details see e.g., Andrews et al., 1987; Oberländer-Hayn et al., 2015; Delaygue et al., 2015; Spiegl et al., 2022). The tropopause acts as a barrier for the vertical transport towards the troposphere and causes e.g., Beryllium-10 (hereafter ^{10}Be, half-life of 1.387 million years) to form a stratospheric reservoir above the tropopause, where it resides for around 1–2 years on average before entering the troposphere by stratosphere-troposphere exchange (STE) processes such as tropopause foldings (Feely et al., 1966; Beer et al., 2012; Spiegl et al., 2022). For ^{7}Be however, the formation of a reservoir and long residence times in the stratosphere are counteracted by the much shorter half-life of the nuclide. Therefore, only ^{7}Be that enters the troposphere shortly after production can be transported from the stratosphere to the surface, which makes ^{7}Be a good indicator for STE (Terzi and Kalinowski, 2017). The transport towards the surface in the troposphere is determined by vertical convective transport, e.g., at the Hadley-Ferrel convergence zone (HFCZ) or due to the El Niño Southern Oscillation (ENSO) related equatorial Walker Circulation, as well as by synoptic dynamics and small-scale convective mixing. The residence time for aerosols in the troposphere ranges from a few weeks to a few days, depending also on the size of the aerosols (Yamagata et al., 2019).

The deposition of ^{7}Be within the troposphere comes from wet deposition such as impact scavenging (wash out of ^{7}Be due to convective precipitation, e.g., at the intertropical convergence zone (ITCZ), and large-scale precipitation) and nucleation scavenging, which describes the dissolution of aerosol particles into water droplets inside clouds (in-cloud scavenging), during the nucleation and growth of cloud droplets by microphysical processes that can result in precipitation formation (Tost et al., 2006; Ohata et al., 2016). Close to the surface ^{7}Be is also deposited by dry deposition and sedimentation (depending on the size of

* Corresponding author. Carl-Heinrich-Becker-Weg 6-10, 12165, Berlin, Germany.
E-mail address: schaak88@zedat.fu-berlin.de (K. Schaar).

https://doi.org/10.1016/j.jenvrad.2024.107592
Received 19 October 2024; Received in revised form 26 November 2024; Accepted 26 November 2024
Available online 9 December 2024

the coupled aerosols).

The various factors of production (phase of the 11-year solar cycle), transport (e.g., intensity of STE and ENSO) and deposition (e.g., wash out due to precipitation) of ^{7}Be are all imprinted in the concentration of near-surface ^{7}Be, making ^{7}Be measurements at ground level a suitable instrument for studying atmospheric dynamics on the time scale of its half-life (Terzi and Kalinowski, 2017). Such studies e.g., have been conducted by Taylor et al. (2016), who explained the variability of ^{7}Be at sampling sites in England (Plymouth and Chilton) and Wales (Aberporth) during 2009 and 2010 by precipitation dynamics and identified STE and convective circulation within the troposphere as factors influencing the near-surface ^{7}Be concentration. Another study by Neroda et al. (2016) showed that seasonal variations of ^{7}Be in Vladivostok (Russia) during 2013 and 2014 are strongly influenced by the direction and height of incoming air masses, thus atmospheric circulation. In a more global study Terzi and Kalinowski (2017) used ground level ^{7}Be data at 63 globally distributed locations from the international monitoring system (IMS) of the Comprehensive Nuclear-Test-Ban Treaty Organization (CTBTO) to reconstruct the global signature of the ITCZ, HFCZ and Polar-Ferrel convergence zone (PFCZ). Furthermore, the authors highlight in this study correlations and preliminary findings with several atmospheric phenomena such as tropopause height, ENSO, quasi-biennial oscillation (QBO) or Indian monsoon, which also motivated this study. In another study Terzi et al. (2019) present an empirical method, based on the aforementioned global ground level ^{7}Be data, to predict the start, withdrawal and intensity of the Indian monsoon season. With this method, the authors claim that the onset can be forecasted with an unprecedented accuracy of ±3 days, 2 months in advance compared to 1–3 weeks in advance by traditional methods. The ground level ^{7}Be data used in Terzi and Kalinowski (2017) as well as in Terzi et al. (2019) have also been used for comparison in this paper and will be explained in the next section.

Although all the aforementioned empirical studies show interesting and important results, they are either limited to single locations, not particular suitable to investigate atmospheric phenomena on a larger scale through ^{7}Be, or are limited in time, not covering periods long enough to investigate atmospheric phenomena with longer oscillation periods like e.g., ENSO. Therefore, and to add a modelling perspective to the debate, the authors of this study carried out global ^{7}Be passive tracer experiments for the period 1850–2100 with the chemistry-climate model ECHAM/MESSy Atmospheric Chemistry (EMAC) (Jöckel et al., 2016), that has been successfully used in former studies to model the production, transport and deposition of cosmogenic Beryllium (e.g., Spiegl et al., 2022; Schaar et al., 2024). The aim is to gain a deeper understanding of the variability of the concentration of near-surface ^{7}Be due to different factors. In this study we focused on ENSO and the impact of the different ENSO phases El Niño, La Niña and neutral on the variability of near-surface ^{7}Be. ENSO is particularly interesting because it is a complex tropical climate phenomenon that arises from irregular variations in winds and sea surface temperatures over the tropical Pacific and affects much of the climate in the tropics and subtropics as well of regions in higher latitudes due to teleconnections (Bjerknes, 1969). By studying the variability of near-surface ^{7}Be due to ENSO, we can determine how the changes in the precipitation pattern and the associated atmospheric circulation, e.g., the Walker Circulation, of the respective ENSO phase alters the concentration of near-surface ^{7}Be, and additionally explore what could be learned from ^{7}Be measurements about ENSO. One typical indicator of the ENSO phase is the Southern Oscillation Index (SOI, see e.g., Ropelewski and Jones, 1987), or the improved equatorial SOI (EOI), which is based on the zonal gradient of sea surface pressure between the western Pacific (5°N–5°S, 90°E−140°E) and eastern Pacific (5°N–5°S, 80°W–130°W) along the equator (Shi and Su, 2020). Also, other indices, e.g., the NINO3.4-index, which is based on sea surface temperatures, are used to define the phase of ENSO, however not required for the context of this study and therefore not considered. The SOI and EOI used in this paper are standardized as such, that the threshold for the El Niño is −7 and 7 for La Niña.

Before the simulations conducted for this study are explained (Section 2), the results are shown and discussed (Section 3) and the conclusion is presented (Section 4), we briefly describe the ground level ^{7}Be data from the IMS of the CTBTO used in this paper for comparison to the results of the model (Section 3).

The CTBTO has built up a global network of stations that collect daily samples of ground level air to measure radionuclide concentrations, such as the concentration of near-surface ^{7}Be. This is the IMS network and the ^{7}Be data of the IMS has been successfully used in former studies, e.g., Terzi and Kalinowski (2017), Terzi et al. (2019, 2020), to show correlations between ground level ^{7}Be and atmospheric circulation. In this study, we use the IMS data to compare the measurements from specific stations with results from our simulations. This is on the one hand a validation of our simulations and provides on the other hand an opportunity to gain a better understanding of what the IMS data shows and what potentially could be done with it. Note that the CTBTO is not responsible for the views of the authors and not necessarily agrees with them.

2. Model setup and methods

As in Schaar et al. (2024), passive tracer experiments were carried out with the chemistry-climate model EMAC (Jöckel et al., 2016), which is based on the European Centre Hamburg general circulation model 5 (ECHAM5) (Roeckner et al., 2006) and the modular Earth submodel system (MESSy) model version 2.55. The MESSy interface (Jöckel et al., 2010) is a modular submodel system that allows the simulation of various chemical and physical processes that are important for the transport and deposition of cosmogenic nuclides. The simulations were conducted using a horizontal/vertical resolution of T42L47MA, corresponding to a Gaussian grid of 2.8 by 2.8° in latitude and longitude (triangular spherical harmonics truncation of T42) and 47 layers in height (L47), with the model upper boundary at 0.01 hPa (~80 km, middle atmosphere). To describe the processes specific to our simulations on cosmogenic ^{7}Be, we incorporate several MESSy modules, explained in the following sections.

2.1. *^{7}Be from GCR and aerosol tracer description*

Cosmogenic ^{7}Be is introduced to our simulations in the same way as in Schaar et al. (2024): the 3-dimensional GCR-production rates of ^{7}Be used as input data for our simulations have been calculated using the Particle and Heavy Ion Transport code System (PHITS) based Analytical Radiation Model in the Atmosphere (PARMA) approach, coupled with their production cross sections from atmospheric constituents (^{14}N and ^{16}O) evaluated by PHITS (Sato et al., 2018). See also https://phits.jaea.go.jp/expacs/and https://phits.jaea.go.jp/for further information, Sato et al. (2008) and Sato (2015, 2016) for information on PARMA and Lifton et al. (2014) for information on the application of PARMA for cosmogenic nuclide production.

The data contains the daily production rate of ^{7}Be for the first of each month for the time span 1950 to 2020 (e.g., January 1, 1950, February 1, 1950, March 1, 1950, etc.), which is representative for every day of this time span, because on average the daily variations of global GCR production are small compared to annual and decadal variations. The production rate of ^{7}Be of future time spans is not known, but we assume it to be similar to the present production rates and therefore use the rates from the period 2009–2020 to periodically extrapolate the production of ^{7}Be for 2020–2100. For the same reason, we used the production rate for 2009–2020 for the preindustrial time span 1850–1950, which also allows the comparison between the preindustrial and future time spans. The precalculated 3-dimensional production rates for 1850–2100 are then imported to the model using the OFFEMIS submodel (Kerkweg et al., 2006).

Using this approach, we get an average, global GCR-production rate

of approximately $3{\cdot}10^{17}$ atoms/s, with around 67% of the cosmogenic ^{7}Be being produced above the tropopause on average and the maxima of production located in the mid-latitudes. This agrees with results shown in Golubenko et al. (2022). The production of ^{7}Be runs opposite to the phase of the 11-year solar cycle, with a standard deviation of the production rate of around 10%. Likewise, the amount of ^{7}Be produced in the troposphere ranges from 30% (solar minimum) to 35% (solar maximum). The reason for this is that with changes in the heliospheric shielding within the 11-year solar cycle, also the amount and energy of the GCR particles reaching the atmosphere of the earth varies. The solar modulation potential Φ (which is a parametric representation of the impact of the heliosphere on GCR (Gleeson and Axford, 1968)), is between 400 MV and 1000 MV for 1950–2020 (Usoskin, 2017).

The description of our ^{7}Be tracers is very similar to the description of ^{10}Be in Schaar et al. (2024). ^{7}Be is described as a passive aerosol-like tracer in the model (see Section 1) and to define the physical properties of the tracers, we use the submodel PTRAC (Jöckel et al., 2008), which also includes a simplified aerosol model based on a lognormal distribution representation of the aerosol particle size (equation (1) in Malinina et al., 2018) with mean radius R and standard deviation σ. Like in Schaar et al. (2024), we assume that the isotopes produced above the tropopause couple to a different aerosol distribution than the isotopes produced in the troposphere. ^{7}Be produced above the tropopause is attached to stratospheric aerosols from the Junge layer (e.g., sulfuric acid and water droplets) with an unperturbed size distribution (no volcanic background aerosols) of approximately $R = 0.1$ μm and $\sigma = 1.4$ (Deshler, 2008). ^{7}Be produced in the troposphere is attached to tropospheric aerosols (e.g., water droplets, volcanic aerosols, sea salt, dust, pollen), which range in size from submicron to >100 μm (Pandis et al., 1995). In Schaar et al. (2024), we found the best results according to data comparison for $R = 0.6$ μm and $\sigma = 2.0$ for the size distribution of the tropospheric aerosols, so we use these values again in this study. For the aerosol density, we chose 1500 kg/m^3 for all simulations, to match the typical range (500–3000 kg/m^3) (Kerkweg et al., 2006).

Due to the description of the cosmogenic ^{7}Be as an aerosol tracer, the deposition processes (wet and dry deposition and sedimentation) for aerosols apply. Sedimentation due to gravitational settling of the aerosol particles throughout the whole atmosphere is considered using a zeroth order upwind scheme (implemented in the submodel SEDI (Kerkweg et al., 2006)) with a sedimentation velocity based on the Stokes velocity corrected for aspherical particles (Kerkweg et al., 2006). Wet deposition is described by the submodel SCAV (Tost et al., 2006) incorporating impact scavenging and nucleation scavenging (for more details see Tost et al., 2006). Dry deposition of ^{7}Be containing aerosol particles is applied at the lowest model level, using the submodel DDEP (for more information about DDEP see Kerkweg et al. (2006)).

The half-life period of ^{7}Be of about 53 days was implemented using the submodel TREXP (Jöckel et al., 2010).

2.2. Description of transient ^{7}Be simulations from 1850 to 2100

We performed transient passive tracer simulations from 1850 to 2100 with interactive chemistry switched off (EMAC in GCM mode) and a coupled ocean using the submodel MPIOM (Pozzer et al., 2011). The boundary conditions for greenhouse gas (GHG) concentrations are prescribed according to the Coupled Model Intercomparison Project 6 (CMIP6), using the shared socio-economic pathway 3–7.0 (SSP3-7.0) scenario, where the approximate level of radiative forcing resulting from the scenario in the year 2100 is 7.0 W/m^2 (Meinshausen et al. (2020). We choose this scenario with high GHG emissions, according to the intergovernmental panel on climate change sixth assessment report (IPCC et al., 2023), to effectively study possible future changes of the transport of ^{7}Be. The initial conditions for the ocean (MPIOM) and the boundary conditions for ozone were prescribed from transient simulations within the Solar Contribution to Climate Change on Decadal to Centennial Timescales project (SOLCHECK), representing the years from 1850 to 2100, with interactive ozone chemistry and ocean coupling to MPIOM. The solar forcing for the SOLCHECK runs was chosen according to the recommendations of the SOLARIS-HEPPA initiative (Matthes et al., 2017). We prescribed ozone fields and did not use interactive chemistry, because this does not affect our ^{7}Be but reduces computational time and required storage resources considerably.

In summary, we conducted an ensemble of 10 250-year simulations. Thus, a total of 2500 model years have been analyzed. During each simulation, ^{7}Be is continuously produced according to the prescribed time-varying GCR production rate time series, as described in Section 2.1.

2.3. Baxter-King bandpass filter, additive decomposition and fourier transformation of ^{7}Be time series

For the analysis of the ^{7}Be time series we used the Baxter-King bandpass filter, additive decomposition and Fourier transformation to extract periodic changes in the ^{7}Be signals, e.g., from annual variability, the 11-year solar cycle or ENSO. The Baxter-King bandpass filter is a bandpass filter with a lead-lag length as well as a minimum and maximum period to pass, and was implemented according to Baxter and King (1999). The additive decomposition, where the time series is decomposed into a sum of a trend, a seasonal component and a residuum, was obtained by first estimating the trend by applying a convolution filter to the data. In the next step, the trend is removed from the series and the average of this de-trended series for each period is then returned as the seasonal component, whereas the rest is considered the residuum. For the Fourier transformations we used the Fourier transformation functions of the well-established SciPy package in python (Virtanen et al., 2020).

3. Results and discussion

From our simulations, we obtain the time series of the concentration of ^{7}Be for every lowest grid point, representing near-surface ^{7}Be, of all 64 latitudes and 128 longitudes over the time span from 1850 to 2100 in monthly resolution.

3.1. Analysis of simulated near-surface ^{7}Be time series

As an example, Fig. 1 shows the ^{7}Be time series for the grid point nearest to the IMS station RN09 (Darwin, Northern Territory (NT), Australia) compared to the ^{7}Be data measured at this station. We choose this station here because it is located within the main meteorological impact area of ENSO.

Fig. 1 shows a good qualitative agreement between the simulation and measured data for station RN09. Both the same annual variability, basically based on the annual precipitation, as well as the variability of the ^{7}Be production due to the 11-year solar cycle, which e.g., causes an underlying slower oscillation of the ensemble mean. To systematically investigate the different factors impacting the ^{7}Be time series at this grid point and station, we applied a Fourier transformation to the time series and try to identify different periodic influences. For this analysis, we chose the simulated time series for the preindustrial era from 1850 to 1950 to neglect influences from climate change.

The Fourier spectrum of the time series shown in Fig. 2 reveals, that the concentration of near-surface ^{7}Be at RN09 is likely to be influenced also by ENSO and the QBO, which cannot directly be interfered from the time series itself. This analysis is now applied to all ^{7}Be time series from 1850 to 1950 at all grid points near the surface, to systematically map the amplitude of the near-surface ^{7}Be variability resulting from the annual cycle, the 11-year solar cycle, QBO and ENSO. Fig. 3 shows the results of this analysis as global maps.

The annual variability of ^{7}Be shown in Fig. 3 (ANNUAL CYCLE) can be explained by two factors: a) the amount of ^{7}Be reaching the surface due to production and transport, and b) precipitation (wash out due to

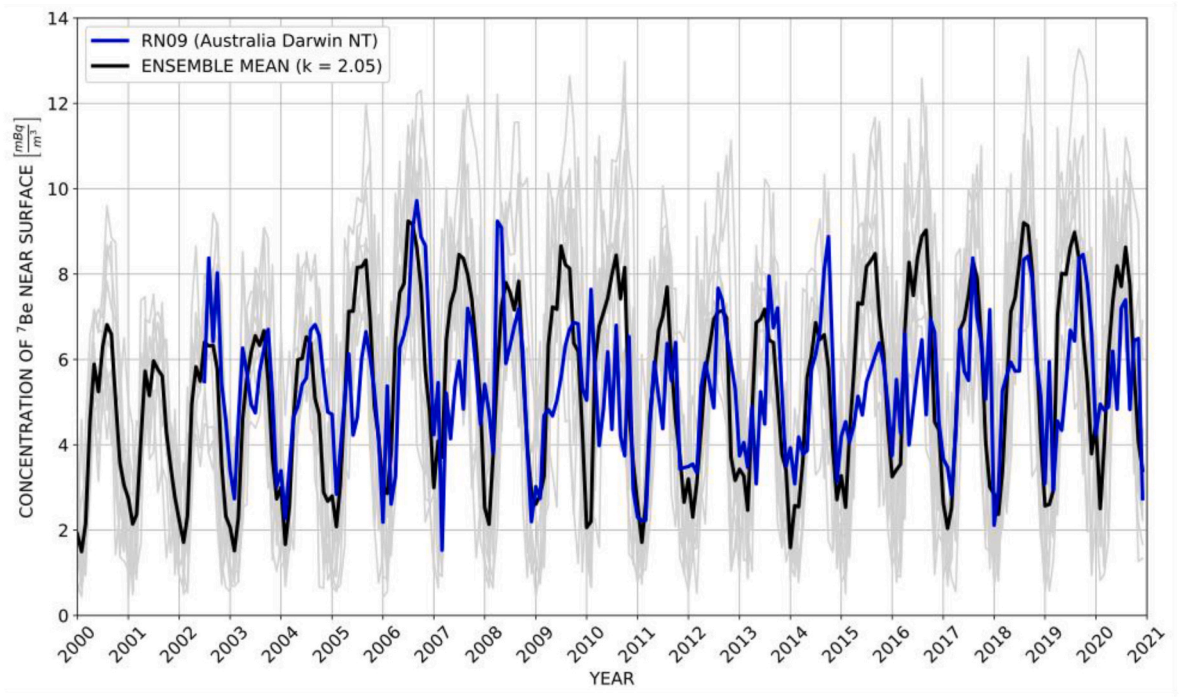

Fig. 1. Comparison of the simulated time series of the concentration of near-surface ^{7}Be in monthly resolution for the years 2000–2021 with data from the IMS station RN09. The black line indicates the ensemble mean from the simulations and the light grey lines show the time series of individual ensemble members. The blue line shows the ^{7}Be data measured at the station RN09. The mean of the ensemble mean is matched to the mean of the measured data by a simple scaling factor k, that accounts for the fact that the grid point covers a much larger area than the station. The Pearson correlation coefficient (PCC) between the simulation and the IMS data is 0.58 and 0.83 when looking at seasonal means (PCC-Seasonal, seasonal mean for every month). (For interpretation of the references to colour in this figure legend, the reader is referred to the Web version of this article.)

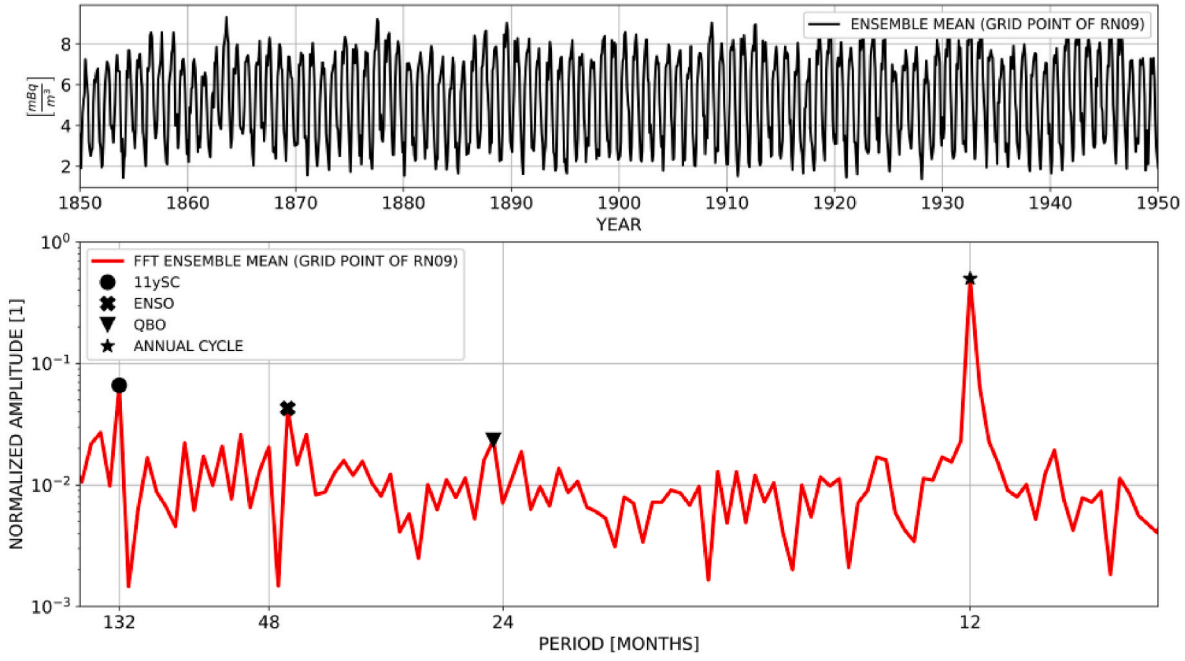

Fig. 2. Top: Ensemble mean of the ^{7}Be time series at the grid point of RN09 for the period 1850–1950. Bottom: Fourier spectrum of the time series shown above. The amplitude of the peaks is normalized to the mean of the time series. Four different peaks are indicated: The 11-year solar cycle (11ySC) with a period of 132 months, ENSO with a period of around 48 months, the QBO with a period close to 24 months and the annual cycle with a period of 12 months.

wet deposition). Close to the equator, the annual variability arises from high precipitation with a strong seasonality due to the motion of the ITCZ, which causes a lot of wet deposition of ^{7}Be by impact scavenging from convective precipitation. At these low latitudes, the mean of the ^{7}Be concentration is lower on average than at higher latitudes because, as for ^{10}Be, the majority of ^{7}Be is produced at higher latitudes due to the morphology of the geomagnetic field and most of the aerosol tracers from the stratosphere enter the troposphere at mid-latitudes (Schaar

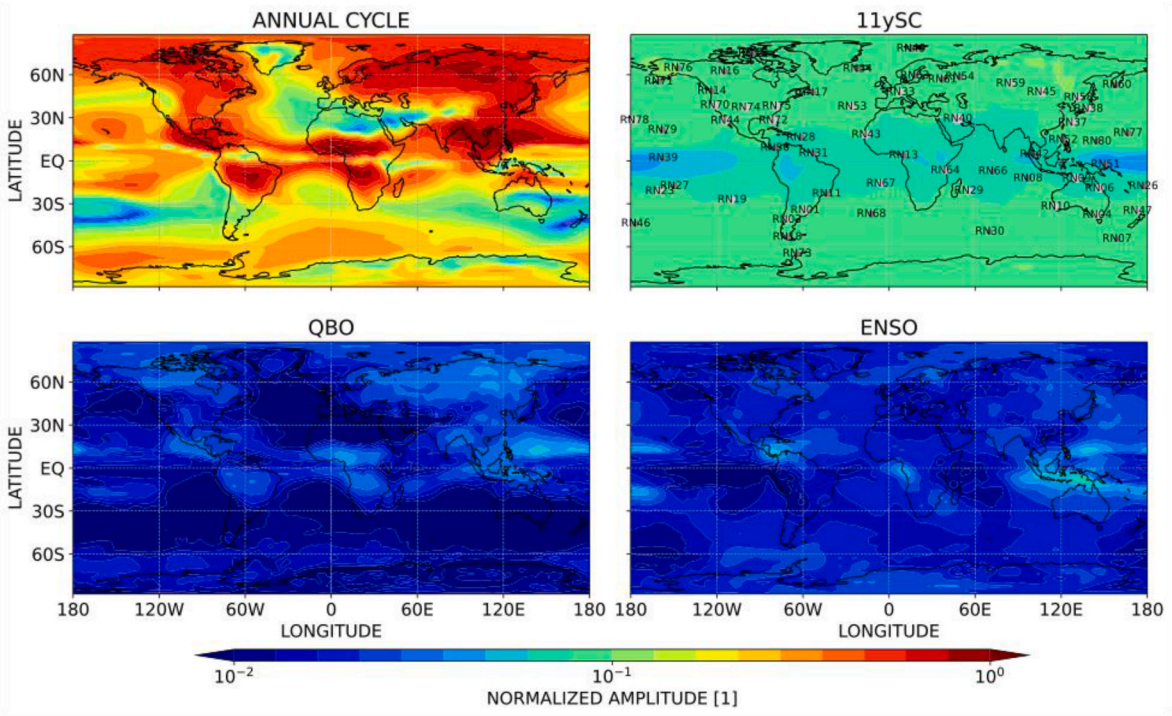

Fig. 3. Global maps of the normalized amplitude of four different peaks of the Fourier spectrum of the near-surface ^{7}Be time series for 1850–1950. The maps indicate the variability of the annual cycle, the variability of the 11-year solar cycle, the impact of the QBO and the impact of ENSO. Within the 11ySC map the positions of the IMS stations are marked.

et al., 2024). Therefore, the annual variability of ^{7}Be close to the surface is high in this region and follows the motion of the ITCZ in Fig. 3. Besides the motion of the ITCZ, also the impact of strong precipitation on ^{7}Be due to the monsoon over southeast Asia and China is visible in the ANNUAL CYCLE panel of Fig. 3. The annual variability at higher latitudes, where more ^{7}Be is produced and most of the tracers are introduced from the stratosphere (30°–70°), can be explained by a) wet deposition due to convective and large-scale precipitation and b) the seasonality of STE, which transports ^{7}Be into the troposphere in the respective winter and spring seasons of the hemispheres. The asymmetry between the NH and the SH, with more annual variability in the NH on average, results from the more pronounced seasonality of wet deposition and a stronger transport by the mean meridional circulation of the BDC in boreal winter and spring relative to the corresponding austral season (Delaygue et al., 2015; Schaar et al., 2024). Note that areas of lower annual variability arise from low precipitation (e.g., Sahel region, Arabic peninsula, or parts of Greenland) or comparatively high mean near-surface ^{7}Be concentrations for the considered time span.

The variability due to the 11-year solar cycle, shown in the panel 11ySC in Fig. 3, is relatively homogeneous with a lower variability at low latitudes than at higher latitudes, following the distribution of ^{7}Be production rates caused by the morphology of the geomagnetic field. The overall variability due to the 11-year solar cycle is around 10% of the mean near-surface ^{7}Be concentration, which is consistent with the variability of the chosen production rates of ^{7}Be within the considered time. Note that in general, the impact of the 11-year solar cycle compared to the annual variability is high where the annual variability is low. This increases slightly with latitude. Thus, for stations in areas of lower annual variability, such as RN53 (Azores), RN40 (Kuwait City, Kuwait) or RN47 (Kaitaia, New Zealand), the signal of the 11-year solar cycle is more visible in the time series of ^{7}Be than for stations outside of such areas (not shown).

The panel QBO in Fig. 3 shows a similar pattern like the ANNUAL CYCLE panel, but with a comparatively small amplitude of below 10% of the mean ^{7}Be concentration and less. The reason for the impact of the QBO on the near-surface ^{7}Be concentration and the similarity to the ANNUAL CYCLE panel could be the impact of the phase of the QBO on STE, which also has an impact on the annual variability. Note also that Kodera et al. (2023) suggest, that the phase of the QBO possibly affects the propagation of the Madden-Julian Oscillation, which has an impact on precipitation over the maritime continent and thus near-surface ^{7}Be. Furthermore, several effects of the QBO on tropospheric circulation are known and QBO-related patterns have been found in different observational measures of tropical convective activity obtained from satellite datasets on e.g., precipitation (see e.g., Haynes et al. (2021) for a detailed review). However, in general it might be difficult to attribute the pattern shown in the panel QBO to the stratospheric QBO, because ^{7}Be has a half-life on the scale of residence within the stratosphere. Additionally, the pattern in the QBO panel could arise from other phenomena e.g., a quasi-biennial oscillation in the tropical troposphere uncorrelated to the stratospheric QBO (Yasunari, 1985) or other periodic variations of the annual variability with an oscillation period of around 24 months.

The panel ENSO shows a pattern with the highest amplitudes in the western tropical Pacific, southeast Asia and Australia, as well as in the eastern Pacific, as one would expect for the variability of near-surface ^{7}Be attributed to ENSO. In Section 3.2 this pattern is analyzed in more detail, to gain a better understanding of the impact of ENSO on the near-surface ^{7}Be concentration.

Fig. 4 shows comparisons of simulated ^{7}Be with measured ^{7}Be data from IMS stations in the typical ENSO area. The four stations (RN51 in Papua New Guinea, RN80 on Upi Guam, RN39 on Kiribati and RN50 in Panama) span a large area and show a good agreement between simulation and measured data. Whereas RN50 and RN80 show a relatively pronounced annual cycle, RN51 and RN39 show a weaker annual cycle because of lower precipitation rates at these stations located close to the equator. The data for RN51 in Fig. 4a (blue line) shows no clear seasonality, but also the results from the simulations (black line) only show a weak annual cycle. Moreover, some slight discrepancy for RN39 in Fig. 4c appears, where the ensemble mean shows two annual maxima,

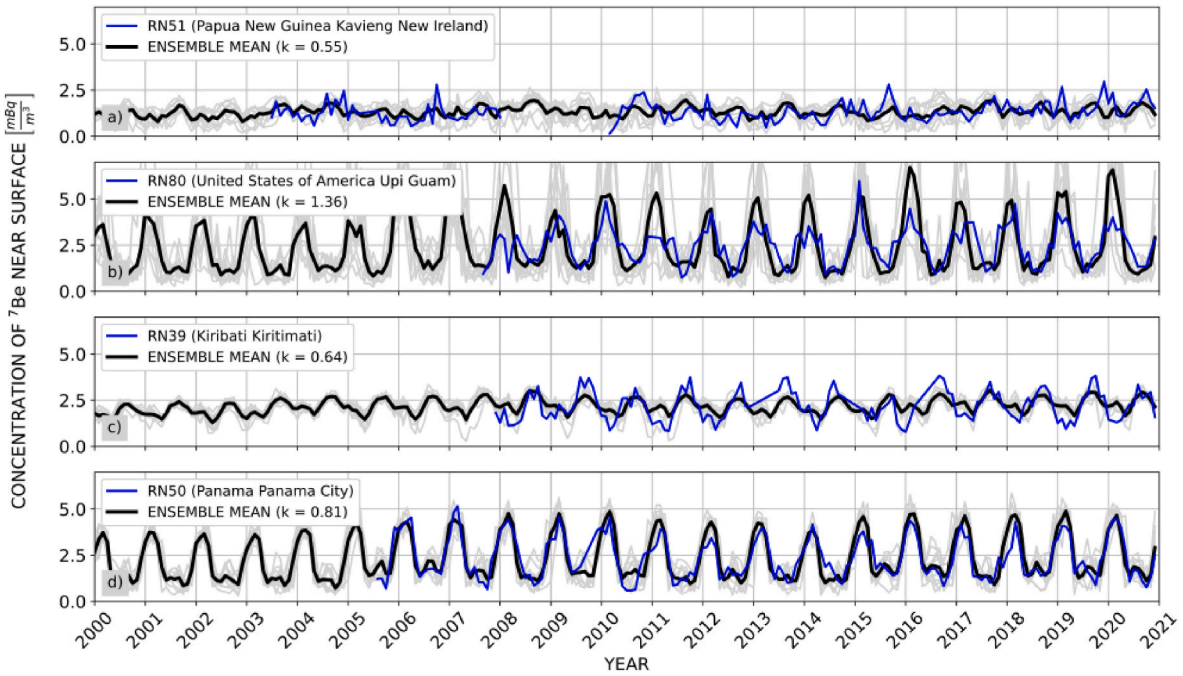

Fig. 4. Comparison of four time series of the concentration of near-surface ^{7}Be in monthly resolution for 2000–2021 with data from four different IMS stations. The depiction in the subplots a) to d) is equivalent to Fig. 1. The PCC and PCC-Seasonal values of the stations are 0.32/0.62 (RN51), 0.72/0.90 (RN80), 0.38/0.61 (RN39) and 0.73/0.74 (RN50).

whereas in the data the smaller maximum is slightly less pronounced. In general, the measured ^{7}Be data from the IMS stations in the ENSO area agree qualitatively well with the results of the simulation.

3.2. *ENSO signatures in near-surface ^{7}Be*

To further analyze and understand the ENSO pattern shown in Fig. 3, we used additive decomposition and Baxter-King bandpass filter on the time series of near-surface ^{7}Be. With this we obtain the time-resolved variability due to ENSO of ^{7}Be. Fig. 5 shows an example, again for

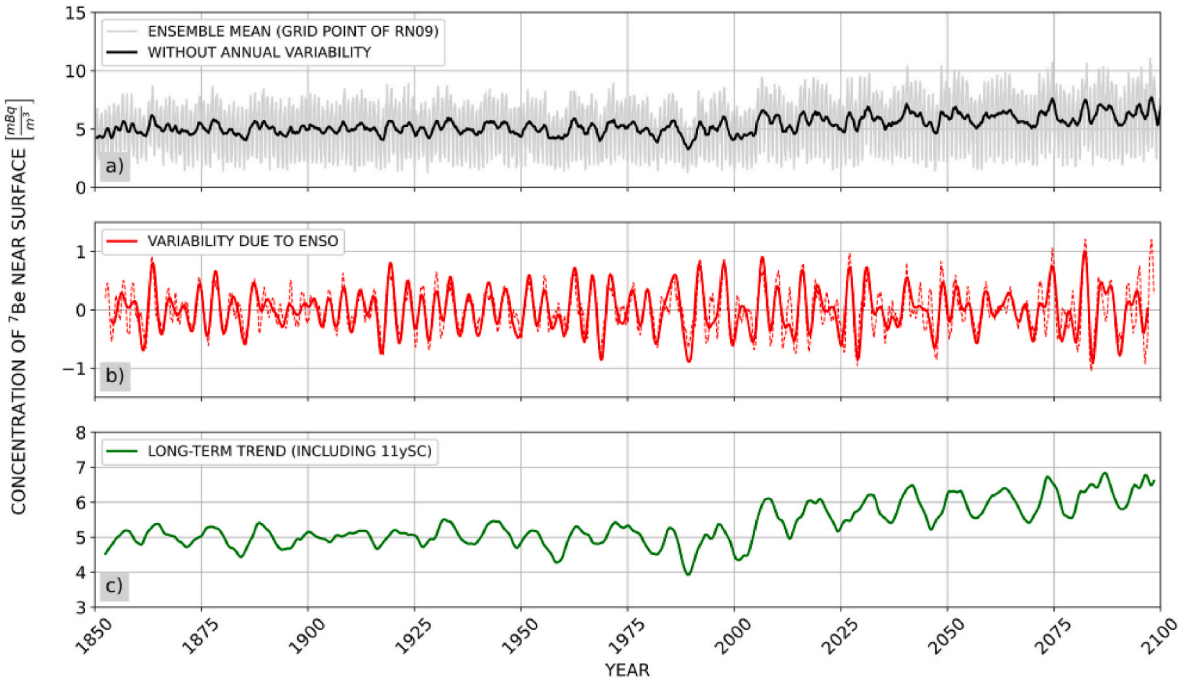

Fig. 5. Panel a) shows the ensemble mean ^{7}Be time series for the grid point nearest to RN09 (Australia Darwin NT) with (light grey) and without (black) annual variability for the whole simulation time span from 1850 to 2100. Panel b) shows the variability of ^{7}Be due to ENSO obtained with the Baxter-King bandpass filter (red) from the ensemble mean shown in a). The dashed line also shows the variability due to ENSO (mainly) but calculated with additive decomposition. The green graph in panel c) shows the variability in the ensemble mean due the 11-year solar cycle as well as climate change (starting approximately after 2000). (For interpretation of the references to colour in this figure legend, the reader is referred to the Web version of this article.)

RN09. The ensemble mean of the ^{7}Be time series in Fig. 5a (light grey graph) is subtracted by the annual variability obtained from additive decomposition to get the ensemble mean without annual variability (black graph in Fig. 5a). The ensemble mean without annual variability can be further subtracted by the background variability from of the 11-year solar cycle plus climate change (trend shown in Fig. 5c) to obtain the variability due to all other modes with a period longer than 12 months, shown by the dashed red graph in Fig. 5b. The red solid line in Fig. 5b is obtained by applying the Baxter-King bandpass filter, with a lead-lag length of 48 months (the period at which ENSO in Fig. 3 was located), a minimum period of 30 months and a maximum period of 108 months to pass, on the ensemble mean in Fig. 5a (note that the result is robust against variations of the minimum and maximum period as long as the periods are above 24 month and below 11 years). The result of the red solid graph and the red dashed graph are very similar, indicating that the variability due to higher modes than annual mainly comes from ENSO for this grid point. However, the results from the Baxter-King band pass filter are slightly cleaner, also excluding the small impact from the QBO. Therefore, this method is used for the following analysis.

The Baxter-King bandpass filter analysis to get the variability due to ENSO (red graph Fig. 5b), was performed for all grid points and all ensembles individually to obtain time-resolved global maps of the variability of ^{7}Be due to ENSO, representing the ENSO signatures in near-surface ^{7}Be. Fig. 6 shows the result for one specific month in the preindustrial time span from 1850 to 1950, which we consider here first to neglect the impact of climate change on the ENSO pattern.

The global map of the ^{7}Be variability due to ENSO (short ^{7}Be-ENSO map) in Fig. 6 is shown for the September 1, 1915, where the SOI and EOI are below the chosen El Niño threshold of −7. The corresponding pattern of the ^{7}Be-ENSO map depicts a reduction of the near-surface ^{7}Be concentration over the tropical Pacific in the area surrounding RN51 and RN39. In contrast, ENSO increases the concentration of ^{7}Be in maritime continent and Australia (e.g., RN09 and RN06). Other, more subtle, impacts of ENSO on ^{7}Be can be observed, e.g., over Panama (RN50, increase), the west coast of the United States and Canada (RN70 and RN14, increase), Alaska (RN76, decrease) or Cape Horn (RN18, increase).

To systematically investigate the pattern for El Niño conditions shown in Fig. 6 and to understand the underlying meteorological processes shaping this pattern, we calculated the mean of all ENSO signatures in near-surface ^{7}Be for which the EOI is below −7 (all time steps with EOI < −7) for all ensemble members. The result is shown in Fig. 7b. Additionally, Fig. 7 shows the results for El Niño conditions (EOI < −7) versus the mean for the 1850–1950 average over all ensemble members for the ^{7}Be concentration above the equator and vertical wind speed (Fig. 7a) and precipitation (Fig. 7c) to explain the ^{7}Be pattern depict in 7b meteorologically. Fig. 7a indicates that the change of the Walker Circulation during El Niño results in downward transport of ^{7}Be tracer above the equator in southeast Asia, leading to a higher concentration of ^{7}Be in the atmosphere. This, in combination with the relative reduction of precipitation due to El Niño in that area, shown in Fig. 7c, results in the red U-shaped increase of near-surface ^{7}Be concentration for the El Niño phase in Fig. 7b. In contrast, the reduction of ^{7}Be over the Pacific, visible in Fig. 7b, comes from the massive increase of precipitation and thus wash out of near-surface ^{7}Be in this area due to El Niño (Fig. 7c) in combination with increased upward transport, additionally lowering the ^{7}Be concentration in the atmosphere above (Fig. 7a).

Based on the simulations, stations in the main impact area of El Niño experiencing a reduction due to this ENSO phase, like RN39 and RN51, will face a reduction of 5%–25% in near-surface ^{7}Be. The IMS stations in the U-shaped area of increased ^{7}Be concentration due to El Niño show an increase of around 5% (RN23) up to 30% (RN80). In the eastern part of

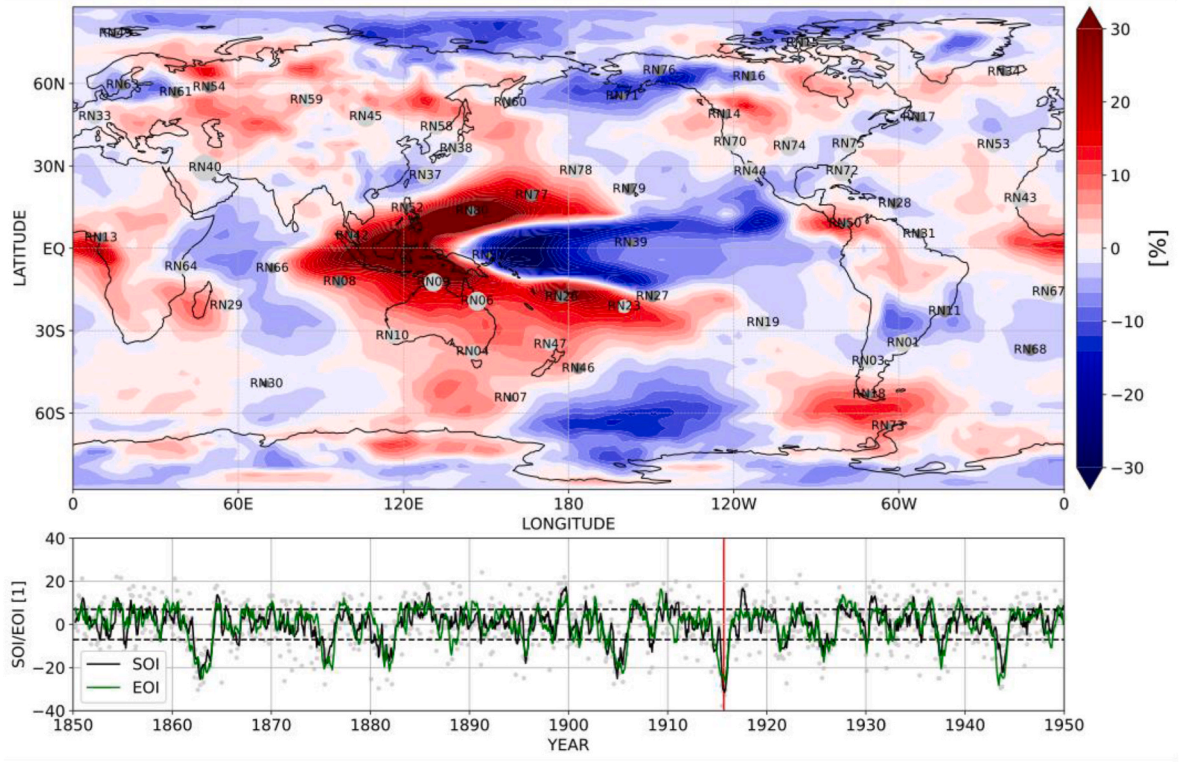

Fig. 6. The upper panel shows the ^{7}Be variability due to ENSO on the September 1, 1915 for ensemble member 1 relative to the mean ^{7}Be concentration in 1850–1950, and the position of the IMS stations. The lower panel shows the SOI (black) and the EOI (green) as a running mean (4 months) for 1850–1950. The red vertical line indicates the date shown in the upper panel. The grey dots show the monthly values of the SOI and the dashed horizontal lines indicate the La Niña (7) and El Niño (−7) thresholds of the SOI and EOI. (For interpretation of the references to colour in this figure legend, the reader is referred to the Web version of this article.)

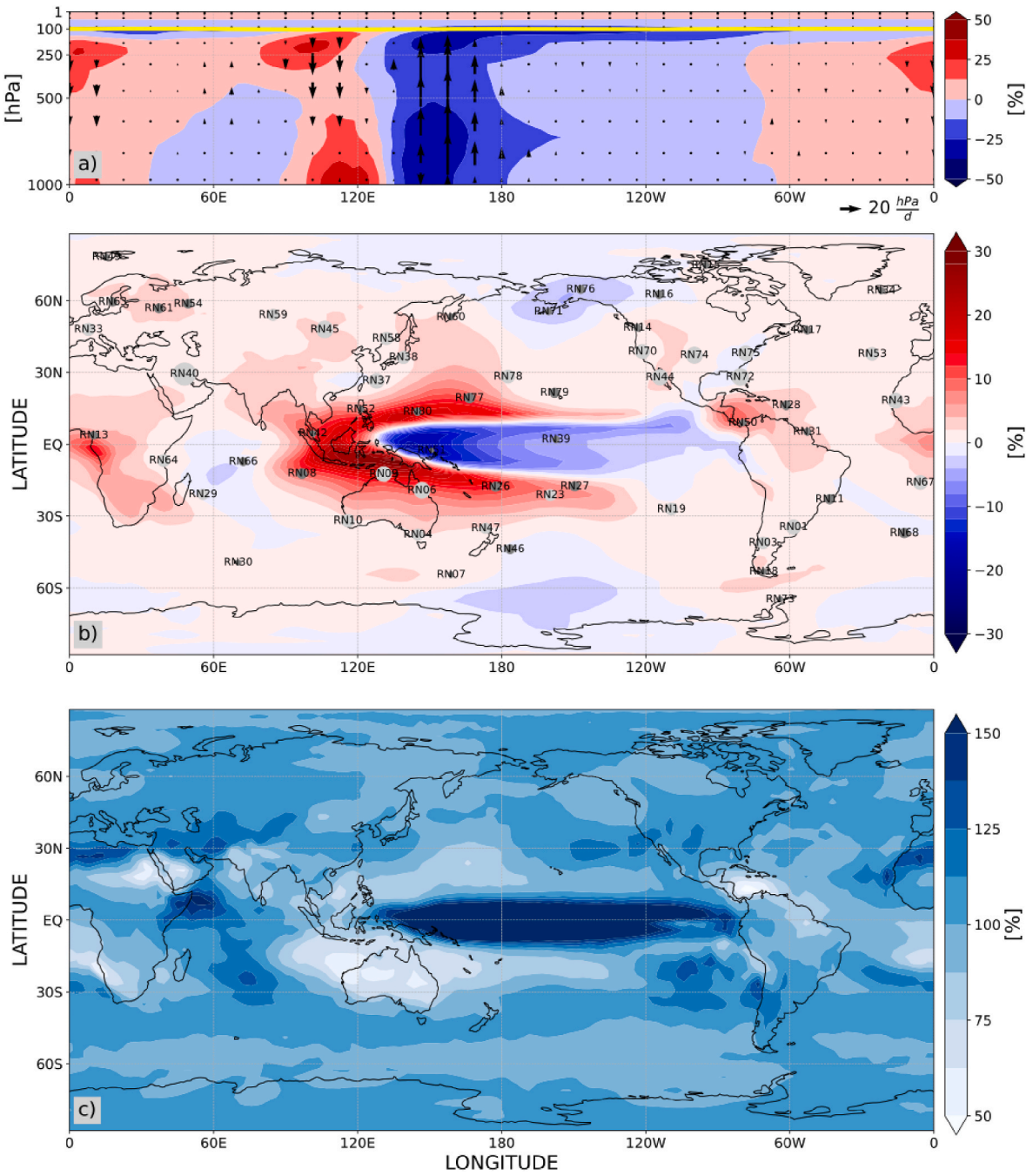

Fig. 7. Panel a) shows a zonal plot along the equator over height for ^{7}Be concentration deviations. The arrows show deviations of the vertical windspeed, indicating up- and downward transport of ^{7}Be. The yellow line represents the tropopause. Panel b) shows the ^{7}Be-ENSO map. Panel c) illustrates the precipitation deviations. All three panels show results for El Niño conditions (EOI < -7) versus the mean for 1850–1950 average over all ensemble members. (For interpretation of the references to colour in this figure legend, the reader is referred to the Web version of this article.)

the Pacific (RN50), the increase reaches 10%. Furthermore, Fig. 7b shows some teleconnection of El Niño, decreasing and increasing the near-surface ^{7}Be concentration also in Alaska (RN76 and RN71, decrease around 5%) or central Africa (RN13, increase up to 10%). Interestingly, these variabilities are not correlated to precipitation anomalies, hence they seem to result from changes in atmospheric transport due to El Niño.

Fig. 8 shows the same results as Fig. 7, but for La Niña conditions (EOI >7), which are a inversion of the results for El Niño. Fig. 8a shows that the vertical component of the Walker Circulation under La Niña conditions leads to increased downward transport over the equatorial Pacific, leading to a higher concentration of ^{7}Be in the atmosphere. This, in combination with the relative reduction of precipitation due to La Niña in that area, (Fig. 8c), results in the increase of near-surface ^{7}Be concentration over the Pacific (Fig. 8b). In contrast, the reduction of near-surface ^{7}Be (Fig. 8b) over the maritime continent and southeast Asia comes from the strong increase of precipitation and thus wash out of ^{7}Be near the surface in this area due to La Niña (Fig. 7c) in combination with increased upward transport, additionally lowering the ^{7}Be concentration in the atmosphere above (Fig. 8a). The resulting U-shaped pattern of ^{7}Be reduction in Fig. 8b is almost identical to the U-shaped pattern of ^{7}Be increase in Fig. 7b. However, the La Niña pattern in Fig. 8b is slightly more shifted to the east, because the upward transport in the Walker Circulation for El Niño is slightly more shifted to the west

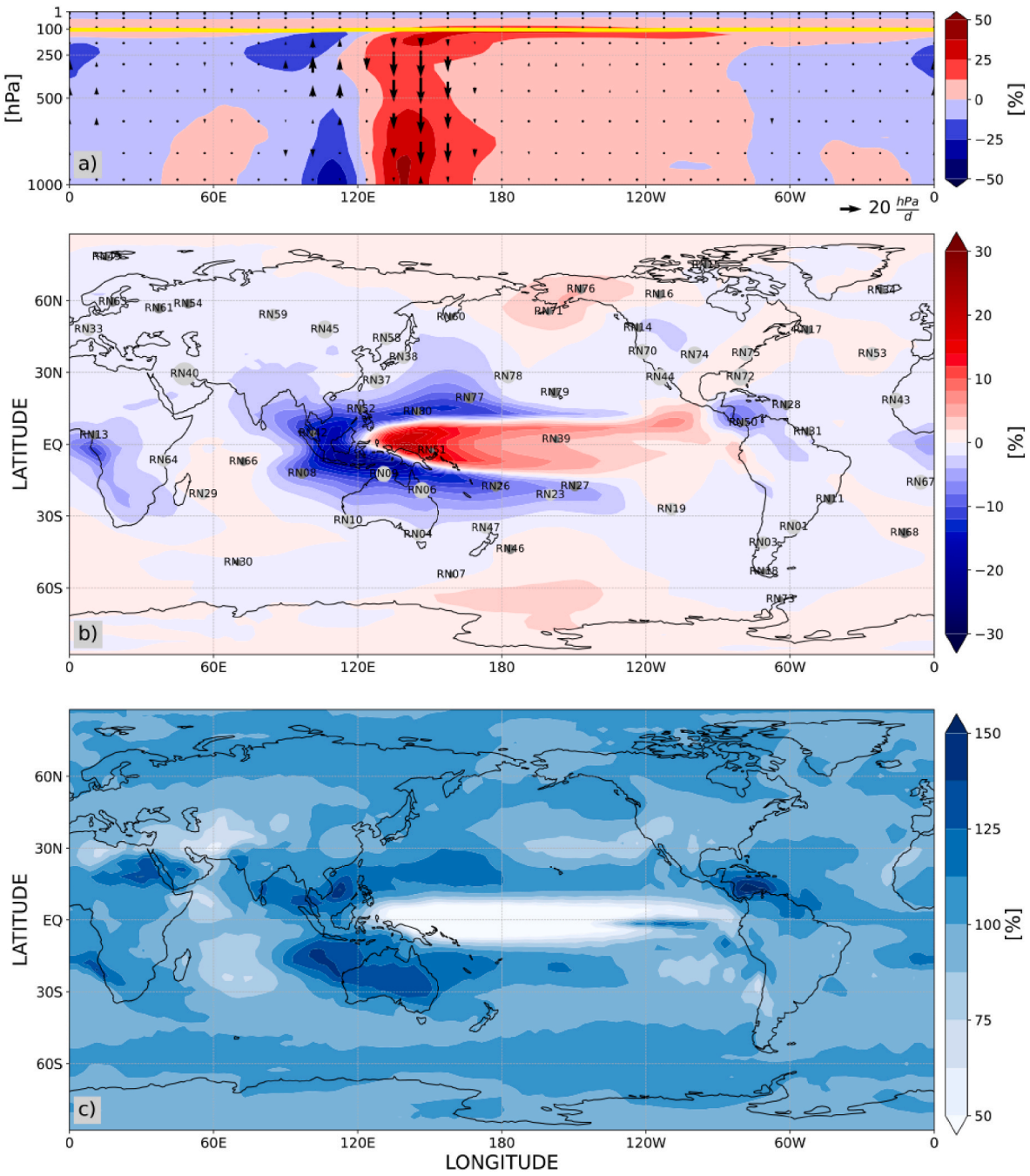

Fig. 8. Same Figure as Fig. 7, but for La Niña conditions (EOI >7).

than the downward transport for La Niña. Furthermore, the overall ^{7}Be reduction inside the U-shaped pattern for La Niña is slightly stronger than the increase in the pattern for El Niño because increase is always limited by the amount of ^{7}Be available, while e.g., wash out due to precipitation can reduce near-surface ^{7}Be until the concentration is close to zero. The teleconnections shown in Fig. 8b are equivalent to Fig. 7b.

Finally, Fig. 9 shows the quantities of Figs. 7 and 8 for neutral conditions, where almost no characteristic ENSO pattern is visible in ^{7}Be (Fig. 9b). The neutral phase is meteorologically a weak La Niña phase and shows a qualitatively similar but much more subtle pattern, with a reduction over the western Pacific in Fig. 9b, which is also consistent with the very weak anomalies shown in Fig. 9a and c. However, note that the area of the reduction is shifted much more east, compared to the La Niña pattern. The anomalies in the precipitation pattern over the central equatorial Pacific in Fig. 9c result from the fact that the precipitation increase from El Niño exceeds the reduction by La Niña, shifting the overall precipitation climatology of this area for 1850–1950 to higher precipitation values than for the neutral phase.

To further evaluate the simulated results presented in Figs. 7–9, Fig. 10 shows a comparison of the simulated variability due to ENSO with IMS data for selected stations within the main impact areas of ENSO for different time spans. The comparison of the simulated variability of near-surface ^{7}Be due to the ENSO phase with ^{7}Be from the IMS stations shows a good agreement for almost all stations. Except for RN27 and RN51, all stations in Fig. 10a follow the El Niño pattern shown in Fig. 7b (dashed red line in Fig. 10a), some also match the calculated values very well. The two stations that differ qualitatively are both located close to the border of the U-shaped El Niño pattern shown in Fig. 7b, which could

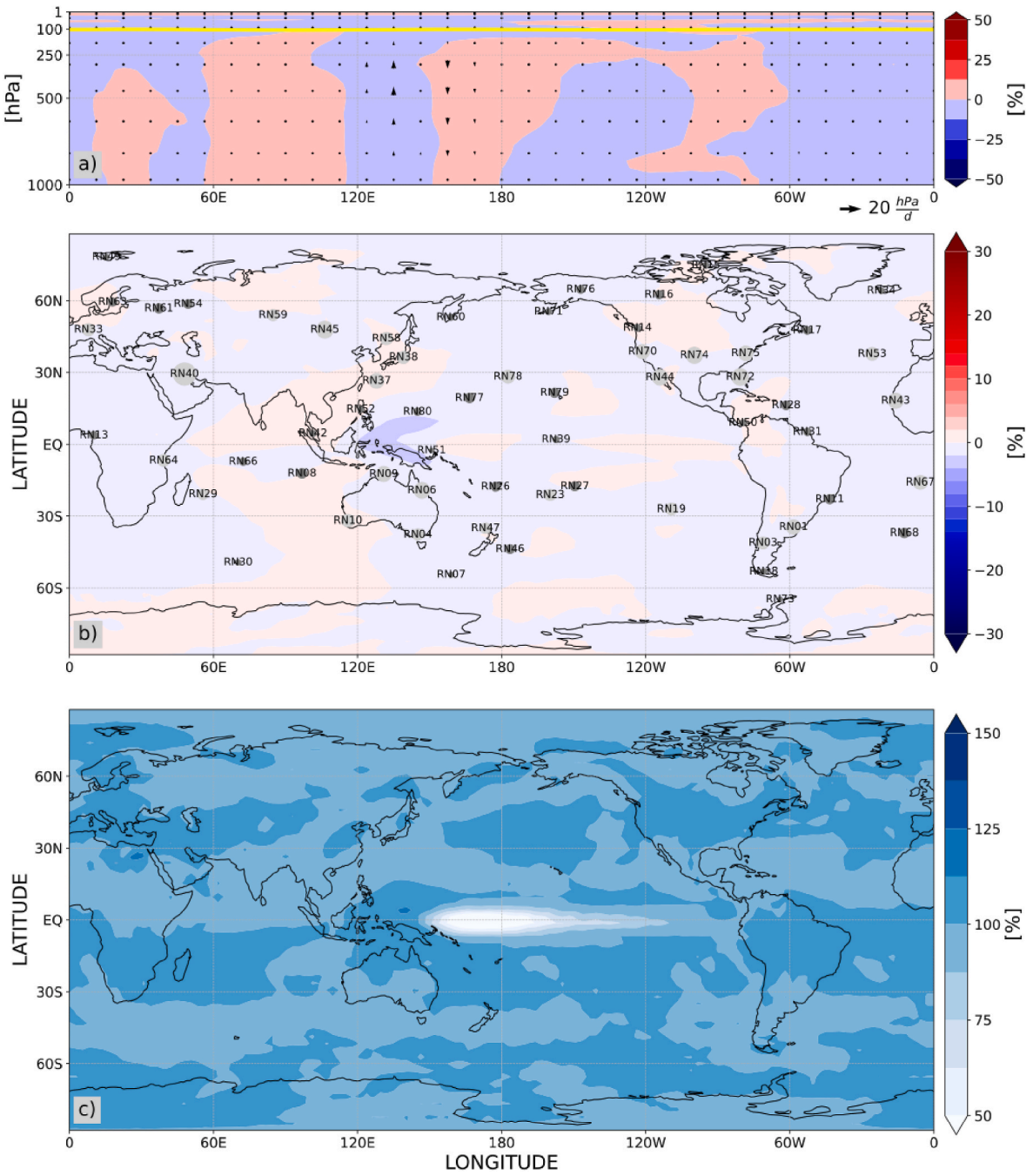

Fig. 9. Same Figure as Fig. 7, but for neutral conditions (EOI <3 and EOI > −3).

explain why the measured data differs from the simulated ensemble mean result. RN51 is very close to the region where the increasing and decreasing factors of ENSO compensate each other (inner border of U-shaped pattern, see Fig. 7b) so the indifference towards the ENSO phase of the real measurements and thus the difference between simulation and data seems plausible. The measurements for RN27 show inverse results relative to the simulated pattern, with a reduction of the near-surface ^{7}Be concentration for the El Niño phase and an increase for the La Niña phase (Fig. 10b). The reason for this is most likely that the tail of the U-shaped pattern shown in Fig. 7b or 8b is an ensemble mean and is located a bit different in real measurements. In Fig. 10b, almost all stations with a positive change due to El Niño show negative changes for La Niña, which supports the results from the simulation. However, the stations in Fig. 10b that are supposed to have positive values according to the simulated pattern for La Niña (RN76, RN39 and RN51), are also negative or close to zero. Besides the explanation for RN51 given before, the reasons for this can be manifold, e.g., too few data from the IMS stations or local specification of the concrete position of the IMS station, that are not captured by the meteorology inside the grid point results to which the data is compared. Also, strong deviations between individual trajectories and the ensemble mean could be an explanation.

Note that the IMS data for some stations is relatively short, including only a few values for El Niño/La Niña phase, which makes the results for the measurements not fully comparable to the simulation. With more data from the IMS network the evaluation will become more reliable. Note also that there are other data sets on ^{7}Be, e.g., from the Environmental Measurements Laboratory's (EML) surface air sampling program, which however contains only some stations with relatively sparse

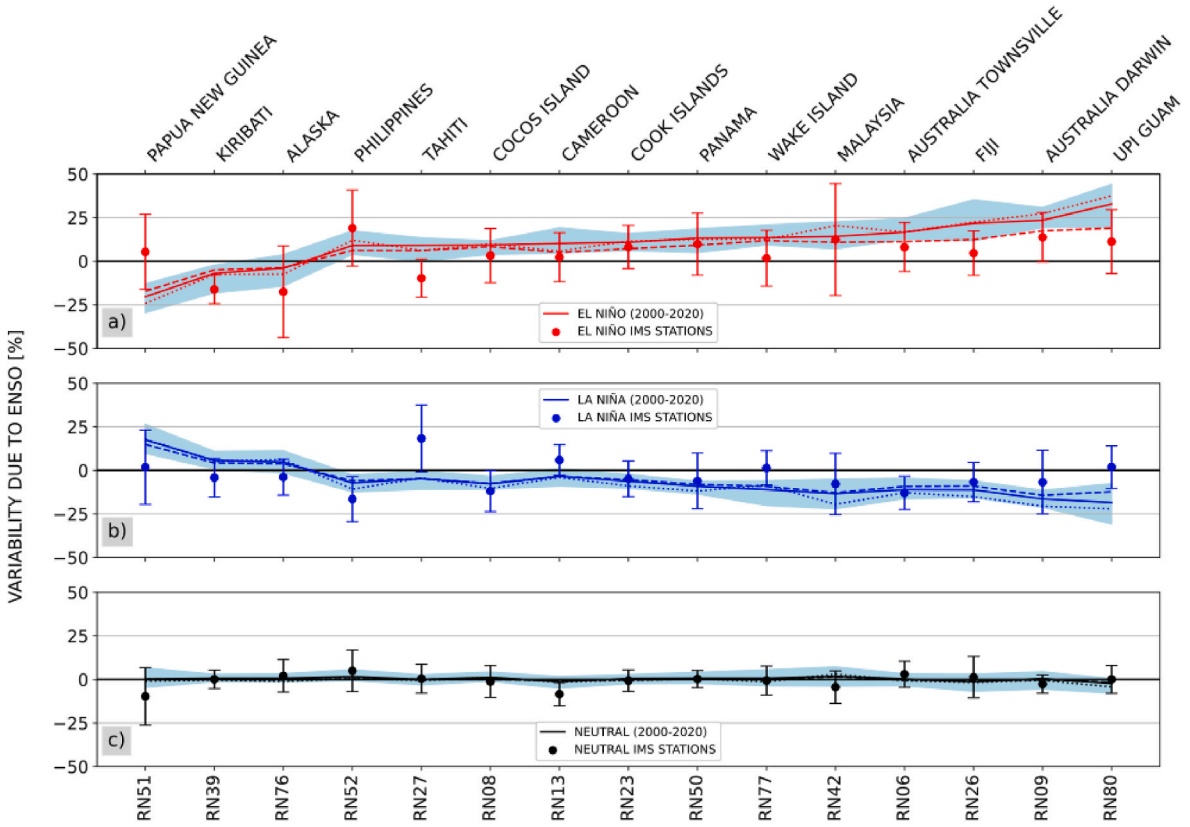

Fig. 10. Comparison of the simulated variability during different ENSO phases with IMS stations most impacted by ENSO in the simulation. Panel a) are the results for El Niño conditions. The red lines show the simulated change in near-surface ^{7}Be at the respective stations for three different time spans, 1850–1950 (dashed, time span shown in Figs. 7–9), 2000–2020 (solid, for comparison with IMS data) and the future period 2050–2100 (dotted). The shaded area indicates the maximum and minimum change in the ensembles for 2000–2020. The red dots depict the measured change due to El Niño, calculated as the mean of the mean concentration for every month with a measured SOI (Ropelewski and Jones, 1987) below −7 (e.g., the mean of the mean concentration of all Januarys/Februarys/ … etc. with SOI < −7). The error bars indicate the standard deviation of the months. The panels b) and c) are the results for La Niña and neutral conditions. Note that the order of the stations on the x-axis is ascending according to values of the solid red line in panel a). (For interpretation of the references to colour in this figure legend, the reader is referred to the Web version of this article.)

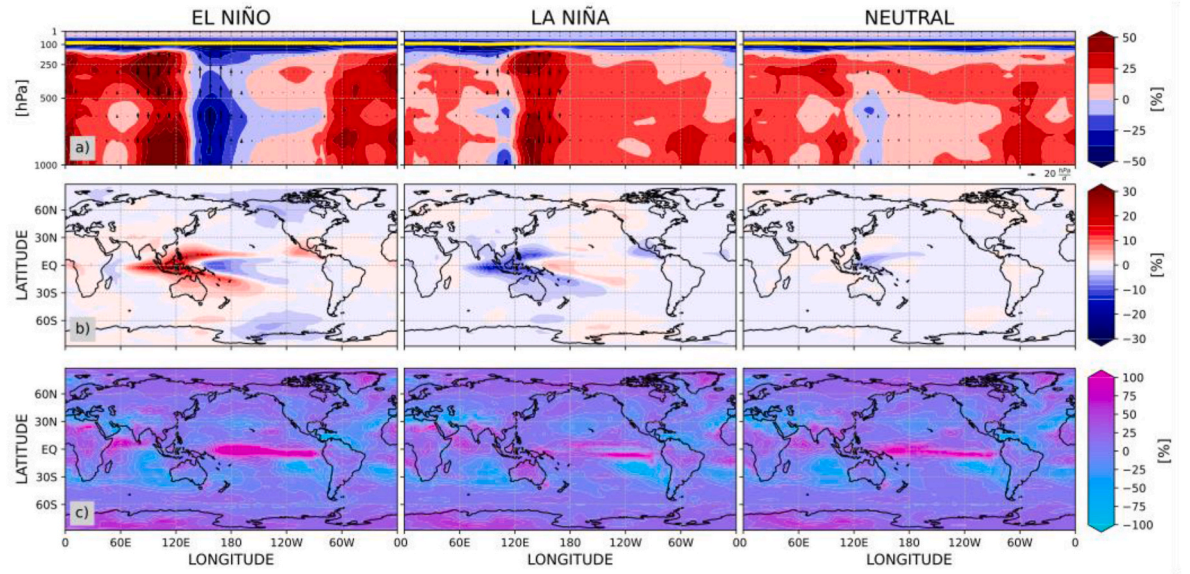

Fig. 11. Row a): Zonal plots along the equator over height for the mean ^{7}Be concentration of 2050–2100 relative to 1850–1950 for El Niño, La Niña and neutral conditions. The arrows show the difference of the vertical windspeed between the two periods, indicating the intensification of up- and downward transport of ^{7}Be. The yellow line represents the mean tropopause height for 2050–2100. Row b): ^{7}Be-ENSO map for 2050–2100 relative to 1850–1950 for the different ENSO phases. Row c): Mean precipitation pattern of 2050–2100 relative to 1850–1950. (For interpretation of the references to colour in this figure legend, the reader is referred to the Web version of this article.)

data relevant to this study. In general, much longer measured near-surface ^{7}Be time series of >50 years (compared to maximum 20 years in Fig. 10) would be required to fully evaluate the results from the simulation. However, as a first empirical comparison the data are helpful and support the results of the simulation. Fig. 10c shows the comparison for neutral conditions for which measurements and simulation results are in good agreement.

3.3. Future projection of ENSO signatures in near-surface ^{7}Be

Fig. 10 also shows the comparison of the ^{7}Be variability due to ENSO for 1850–1950 (dashed line) with 2000–2020 (solid line) and 2050–2100 (dotted line). To further explain the change in the variability and illustrate the respective pattern in ^{7}Be, Fig. 11 depicts the difference between the preindustrial ^{7}Be ENSO pattern (1850–1950) and the future ^{7}Be ENSO pattern, assuming a SSP3-7.0 scenario of GHG emissions (2050–2100).

For El Niño conditions we find that the preindustrial ^{7}Be pattern shown in Fig. 7b is more pronounced and extended towards the Indian ocean for 2050–2100. The reason for this is the increased downward transport by the Walker Circulation in combination with the increased height of the tropopause, which allows for more ^{7}Be in the troposphere above the equator to be transported to the surface before decay (see row a) for El Niño conditions). The future ^{7}Be reduction due to El Niño is driven by the changes in the precipitation pattern over the Pacific shown in row c), which are consistent with the results of the current IPCC report (2023) that expects a further amplification of the rainfall variability related to ENSO in the second half of the 21st century in the SSP3-7.0 scenario.

For La Niña conditions we also find a more pronounced ^{7}Be pattern compared to Fig. 8b, but mostly for the U-shaped reduction area over southeast Asia, which again results from further increased precipitation due to La Niña in this area (Fig. 11c)). For the area in which the near-surface ^{7}Be concentration is increased in Fig. 8b, we only see a slight further increase in 2050–2100 because the increase in downward transport and ^{7}Be concentration in the troposphere above is almost completely compensated by the increase of the precipitation and thus wash out in this area. These counteracting effects also explain the ^{7}Be pattern for neutral condition in Fig. 11. In general, the ^{7}Be concentration in the troposphere is higher compared to 1850–1950 (Fig. 11a) for neutral conditions, but due to higher precipitation this does not translate into higher concentrations of ^{7}Be. The ^{7}Be pattern for neutral conditions in Fig. 11 is just a slightly more pronounced version of the preindustrial pattern shown in Fig. 9b.

4. Conclusion

We used the state-of-the-art chemistry-climate model EMAC combined with input data for ^{7}Be from GCR calculated with PHITS to model the production, atmospheric transport and surface deposition of ^{7}Be from 1850 to 2100 using a SSP3-7.0 GHG scenario. The modelling approach was already developed and successfully utilized for ^{10}Be from GCR and solar energetic particles in Schaar et al. (2024). The model covers the full stratosphere and mesosphere, gives a realistic representation of all major stratospheric and tropospheric dynamics for mass transport, e.g., BDC, STE, planetary wave activity, storm tracks, synoptic dynamics, and incorporates all deposition mechanisms important for the deposition of ^{10}Be, wet and dry deposition and sedimentation.

In this study we concentrated on the variability of ^{7}Be and specifically the impact of ENSO on near-surface ^{7}Be. We found that our model reproduces near-surface ^{7}Be variability in good agreement with ^{7}Be measurements from the IMS network stations of CTBTO. The Fourier analysis and Baxter-King filter analysis of the simulated ^{7}Be time series revealed a strong impact of ENSO on the pattern of near-surface ^{7}Be concentration in the equatorial Pacific. For the El Niño phase, indicated by an EOI < -7, our results show a U-shaped area of enhancement of ^{7}Be over southeast Asia enclosing an area over the equatorial Pacific in which ^{7}Be is reduced. The variability of ^{7}Be is up to ±20% in these two areas, around 10% for Panama (RN50), and up to 5% ^{7}Be enhancement for e.g., India, California and Japan, while the near-surface ^{7}Be concentration in Alaska is reduced due to El Niño. For the La Niña phase, indicated by an EOI >7, we find the same pattern as for the El Niño phase, but inverted. The ^{7}Be pattern for both ENSO phases, as well as for the neutral phase, which is very weak version of the La Niña pattern, can be well understood by the respective anomalies in precipitation and the Walker Circulation. For the future period 2050–2100, we see a further enforcement of the ^{7}Be pattern for El Niño and La Niña relative to the preindustrial era 1850–1950, due to changes in precipitation (concordant with IPCC et al., 2023) and of the Walker Circulation. The pattern for the neutral phase becomes slightly more like the La Niña pattern for 2050–2100. Although the ^{7}Be data of the IMS network stations is yet limited, our model results of the variability of ^{7}Be due to ENSO and the measurements show a good agreement, as depict in Fig. 10. The only exceptions are the stations RN27 and RN51, that are qualitatively different but may depend also on the specific realization compared to measurements.

Possible improvements of our model could be e.g., a more sophisticated aerosol model or a less coarse horizontal resolution to increase precision when comparing simulation results to individual IMS stations or to capture currently sub grid meteorological phenomena, e.g., related to complex topography. However, this will not alter the general findings of this paper.

With this study we provide another example for the potential of using ^{7}Be to study atmospheric phenomena, as already suggested by e.g., Terzi and Kalinowski (2017), but this time from a modelling perspective, revealing the impact of ENSO on ^{7}Be. Further investigation on near-surface ^{7}Be could help to use ^{7}Be as an additional indicator or even predictor of the upcoming ENSO phase, e.g., by calculating the standardized differences of the near-surface ^{7}Be concentration for different stations (e.g., RN09 and RN51, because of the strong gradient between both stations visible in the El Niño and La Niña pattern in Figs. 7 and 8). Furthermore, our results might help to identify IMS stations which are most useful for studying future changes in ENSO due to climate change, e.g., the results depict in Fig. 10 suggest that RN80 (Upi Guam), RN09 (Australia Darwin) or RN39 (Kiribati) show a higher sensitivity to El Niño than other IMS stations and are therefore more suitable for studying El Niño than e.g., RN23 (Cook Islands) or RN77 (Wake Island). Also, the modelling approach used in this study can be employed to study the ^{7}Be variability due to other atmospheric phenomena, such as the QBO, the North Atlantic oscillation or sudden stratospheric warmings. Also, it can be used for a deeper comparison and evaluation of the IMS network data on ^{7}Be, to gain a deeper understanding of the measurements and see what the data could be used for besides the already mentioned phenomena. Furthermore, the extrapolation of the ^{7}Be time series to the future can help to identify which stations are most affected by climate change and thus are most useful to measure and understand climate change from a ^{7}Be perspective.

CRediT authorship contribution statement

K. Schaar: Writing – review & editing, Writing – original draft, Visualization, Validation, Software, Methodology, Investigation, Formal analysis, Conceptualization. **T. Spiegl:** Writing – review & editing, Supervision, Software, Methodology, Conceptualization. **T. Sato:** Resources. **U. Langematz:** Writing – review & editing, Supervision, Conceptualization.

Declaration of competing interest

The authors declare the following financial interests/personal relationships which may be considered as potential competing interests: The Comprehensive Nuclear-Test-Ban Treaty Organization (CTBTO)

data that were used for this study are not publicly available, but access through the virtual Data Exploration Centre (vDEC) can be granted by the CTBTO via a cost-free confidentiality agreement. The application for vDEC access to data can be submitted for approval through a simple web form at https://www.ctbto.org/specials/vdec/. The CTBTO has not influenced the submitted work in any way. Note also that the CTBTO is not responsible for the views of the authors and not necessarily aggress with them. If there are other authors, they declare that they have no known competing financial interests or personal relationships that could have appeared to influence the work reported in this paper.

Acknowledgements

The authors would like to acknowledge the Institute for Space–Earth Environmental Research (ISEE) at the Nagoya University in Japan and the ISEE Joint Research Program for fruitful discussions and scientific exchange, as well as the HLRN supercomputing facility in Berlin for the granted computing time and storage of data. Furthermore, we want to thank the CTBTO for giving us excess to the IMS ^{7}Be data.

Data availability

The amount of model data from the EMAC simulations performed for this study is very large (>1TB) and thus can only be made available on request. The CTBTO data used for this study are not publicly available, but access through the virtual Data Exploration Centre (vDEC) can be granted by the CTBTO via a cost-free confidentiality agreement. The application for vDEC access to data can be submitted for approval through a simple web form at https://www.ctbto.org/specials/vdec/.

References

Andrews, D.G., Holton, J.R., Leovy, C.B., 1987. Middle Atmosphere Dynamics. Academic Press, p. 489.

Baxter, M., King, R.G., 1999. Measuring business cycles: approximate band-pass filters for economic time series. Rev. Econ. Stat. 81 (4), 575–593. https://doi.org/10.1162/003465399558454.

Beer, J., Baumgartner, S., Dittrich-Hannen, B., Hauenstein, J., Kubik, P., Lukasczyk, C., Suter, M., 1994. Solar variability traced by cosmogenic isotopes. Int. Astron. Union Circular 143, 291–300. https://doi.org/10.1017/S0252921100024799.

Beer, J., McCracken, K., Steiger, R., 2012. Cosmogenic Radionuclides: Theory and Applications in the Terrestrial and Space Environments. Springer Science & Business Media. https://doi.org/10.1007/978-3-642-14651-0.

Bjerknes, J., 1969. Atmospheric teleconnections from the equatorial Pacific. Mon. Weather Rev. 97 (3), 163–172. https://doi.org/10.1175/1520-0493(1969)097<0163:ATFTEP>2.3.CO;2.

Delaygue, G., Bekki, S., Bard, E., 2015. Modelling the stratospheric budget of beryllium isotopes. Tellus B 67 (1), 28582. https://doi.org/10.3402/tellusb.v67.28582.

Deshler, T., 2008. A review of global stratospheric aerosol: measurements, importance, life cycle, and local stratospheric aerosol. Atmos. Res. 90 (2–4), 223–232. https://doi.org/10.1016/j.atmosres.2008.03.016.

Feely, H.W., Seitz, H., Lagomarsino, J., Biscaye, P.E., 1966. Transport and fallout of stratospheric radioactive debris. Tellus 18, 316–328. https://doi.org/10.3402/tellusa.v18i2-3.9619.

Gleeson, L.J., Axford, W.I., 1968. Solar modulation of galactic cosmic rays. Astrophys. J. 154, 1011. https://doi.org/10.1086/149822, 154, 1011.

Golubenko, K., Rozanov, E., Kovaltsov, G., Usoskin, I., 2022. Zonal mean distribution of cosmogenic isotope (7Be, 10Be, 14C, and 36Cl) production in stratosphere and troposphere. J. Geophys. Res. Atmos. 127, e2022JD036726. https://doi.org/10.1029/2022JD036726.

Haynes, P., Hitchcock, P., Hitchman, M., Yoden, S., Hendon, H., Kiladis, G., et al., 2021. The influence of the stratosphere on the tropical troposphere. Journal of the Meteorological Society of Japan. Ser. II 99 (4), 803–845. https://doi.org/10.2151/jmsj.2021-040.

IPCC, 2023. Climate change 2023: synthesis report. In: Lee, H., Romero, J. (Eds.), Contribution of Working Groups I, II and III to the Sixth Assessment Report of the Intergovernmental Panel on Climate Change [Core Writing Team. IPCC, Geneva, Switzerland, pp. 35–115. https://doi.org/10.59327/IPCC/AR6-9789291691647.

Jöckel, P., Kerkweg, A., Buchholz-Dietsch, J., Tost, H., Sander, R., Pozzer, A., 2008. Coupling of chemical processes with the modular earth submodel system (MESSy) submodel TRACER. Atmos. Chem. Phys. 8 (6), 1677–1687. https://doi.org/10.5194/acp-8-1677-2008.

Jöckel, P., Kerkweg, A., Pozzer, A., Sander, R., Tost, H., Riede, H., et al., 2010. Development cycle 2 of the modular Earth submodel system (MESSy2). Geosci. Model Dev. (GMD) 3, 717–752. https://doi.org/10.5194/gmd-3-717-2010.

Jöckel, P., Tost, H., Pozzer, A., Kunze, M., Kirner, O., Brenninkmeijer, C.A., et al., 2016. Earth system chemistry integrated modelling (ESCiMo) with the modular Earth submodel system (MESSy) version 2.51. Geosci. Model Dev. (GMD) 9 (3), 1153–1200. https://doi.org/10.5194/gmd-9-1153-2016.

Junge, C.E., 1963. Air chemistry and radioactivity. In: International Geophysics Series, vol. 4. Academic Press.

Kerkweg, A., Buchholz, J., Ganzeveld, L., Pozzer, A., Tost, H., Jöckel, P., 2006. An implementation of the dry removal processes DRY DEPosition and SEDImentation in the Modular Earth Submodel System (MESSy). Atmos. Chem. Phys. 6 (12), 4617–4632. https://doi.org/10.5194/acp-6-4617-2006.

Kodera, K., Nasuno, T., Son, S.W., Eguchi, N., Harada, Y., 2023. Influence of the stratospheric QBO on seasonal migration of the convective center across the Maritime Continent. Journal of the Meteorological Society of Japan. Ser. II 101 (6), 445–459. https://doi.org/10.2151/jmsj.2023-026.

Lal, D., Peters, B., 1962. Cosmic ray produced isotopes and their application to problems in geophysics. Prog. Elem. Part. Cosmic Ray Phys. 6.

Lifton, N., Sato, T., Dunai, T., 2014. Scaling in situ cosmogenic nuclide production rates using analytical approximations to atmospheric cosmic-ray fluxes. Earth Planet Sci. Lett. 386, 149–160. https://doi.org/10.1016/j.epsl.2013.10.052.

Malinina, E., Rozanov, A., Rozanov, V., Liebing, P., Bovensmann, H., Burrows, J.P., 2018. Aerosol particle size distribution in the stratosphere retrieved from SCIAMACHY limb measurements. Atmos. Meas. Tech. 11, 2085–2100. https://doi.org/10.5194/amt-11-2085-2018.

Matthes, K., Funke, B., Andersson, M.E., Barnard, L., Beer, J., Charbonneau, P., Versick, S., 2017. Solar forcing for CMIP6 (v3. 2). Geosci. Model Dev. (GMD) 10 (6), 2247–2302. https://doi.org/10.5194/gmd-10-2247-2017.

Meinshausen, M., Nicholls, Z.R., Lewis, J., Gidden, M.J., Vogel, E., Freund, M., et al., 2020. The shared socio-economic pathway (SSP) greenhouse gas concentrations and their extensions to 2500. Geosci. Model Dev. (GMD) 13 (8), 3571–3605. https://doi.org/10.5194/gmd-13-3571-2020.

Neroda, A.S., Goncharova, A.A., Goryachev, V.A., Mishukov, V.F., Shlyk, N.V., 2016. Long-range atmospheric transport Beryllium-7 to region the Sea of Japan. J. Environ. Radioact. 160, 102–111. https://doi.org/10.1016/j.jenvrad.2016.04.030.

Oberländer-Hayn, S., Meul, S., Langematz, U., Abalichin, J., Haenel, F., 2015. A chemistry-climate model study of past changes in the Brewer-Dobson circulation. J. Geophys. Res. Atmos. 120, 6742–6757. https://doi.org/10.1002/2014JD022843.

Ohata, S., Moteki, N., Mori, T., Koike, M., Kondo, Y., 2016. A key process controlling the wet removal of aerosols: new observational evidence. Sci. Rep.-UK 6, 34113. https://doi.org/10.1038/srep34113.

Pandis, S.N., Wexler, A.S., Seinfeld, J.H., 1995. Dynamics of tropospheric aerosols. J. Phys. Chem. 99 (24), 9646–9659. https://doi.org/10.1021/j100024a003.

Pozzer, A., Jöckel, P., Kern, B., Haak, H., 2011. The atmosphere-ocean general circulation model EMAC-MPIOM. Geosci. Model Dev. (GMD) 4 (3), 771–784. https://doi.org/10.5194/gmd-4-771-2011.

Roeckner, E., Brokopf, R., Esch, M., Giorgetta, M., Hagemann, S., Kornblueh, L., et al., 2006. Sensitivity of simulated climate to horizontal and vertical resolution in the ECHAM5 atmosphere model. J. Clim. 19 (1), 3771–3791. https://doi.org/10.1175/JCLI3824.

Ropelewski, C.F., Jones, P.D., 1987. An extension of the Tahiti-Darwin southern oscillation index. Mon. Weather Rev. 115 (9), 2161–2165. https://doi.org/10.1175/1520-0493(1987)115<2161:AEOTTS>2.0.CO;2.

Sato, T., Yasuda, H., Niita, K., Endo, A., Sihver, L., 2008. Development of PARMA: PHITS-based analytical radiation model in the atmosphere. Radiat. Res. 170, 244–259. https://doi.org/10.1667/RR1094.1.

Sato, T., 2015. Analytical model for estimating terrestrial cosmic ray fluxes nearly anytime and anywhere in the world: extension of PARMA/EXPACS. PLoS One 10 (12), e0144679.

Sato, T., 2016. Analytical model for estimating the zenith angle dependence of terrestrial cosmic ray fluxes. PLoS One 11 (8), e0160390.

Sato, T., Iwamoto, Y., Hashimoto, S., Ogawa, T., Furuta, T., Abe, S.I., et al., 2018. Features of particle and heavy ion transport code system (PHITS) version 3.02. J. Nucl. Sci. Technol. 55 (6), 684–690. https://doi.org/10.1080/00223131.2017.1419890.

Schaar, K., Spiegl, T., Langematz, U., Sato, T., Mekhaldi, F., Kunze, M., et al., 2024. The role of deposition of cosmogenic 10Be for the detectability of solar proton events. J. Geophys. Res. Atmos. 129 (11), e2023JD040463. https://doi.org/10.1029/2023JD040463.

Shi, Y., Su, J., 2020. A new equatorial oscillation index for better describing ENSO and westerly wind bursts. Journal of Meteorological Research 34 (5), 1025–1037. https://doi.org/10.1007/s13351-020-9195-6.

Spiegl, T.C., Yoden, S., Langematz, U., Sato, T., Chhin, R., Noda, S., et al., 2022. Modeling the transport and deposition of ^{10}Be produced by the strongest solar proton event during the Holocene. J. Geophys. Res. Atmos. 127, e2021JD035658. https://doi.org/10.1029/2021JD035658.

Taylor, A., Keith-Roach, M.J., Iurian, A.R., Mabit, L., Blake, W.H., 2016. Temporal variability of beryllium-7 fallout in southwest UK. J. Environ. Radioact. 160, 80–86. https://doi.org/10.1016/j.jenvrad.2016.04.025.

Terzi, L., Kalinowski, M., 2017. World-wide seasonal variation of 7Be related to large-scale atmospheric circulation dynamics. J. Environ. Radioact. 178 (179), 1–15. https://doi.org/10.1016/j.jenvrad.2017.06.031.

Terzi, L., Kalinowski, M., Schoeppner, M., Wotawa, G., 2019. How to predict seasonal weather and monsoons with radionuclide monitoring. Sci. Rep. 9 (1), 2729. https://doi.org/10.1038/s41598-019-39664-7.

Terzi, L., Wotawa, G., Schoeppner, M., Kalinowski, M., Saey, P.R., Steinmann, P., et al., 2020. Radioisotopes demonstrate changes in global atmospheric circulation possibly

caused by global warming. Sci. Rep. 10 (1), 10695. https://doi.org/10.1038/s41598-020-66541-5.
Tost, H., Jöckel, P., Kerkweg, A., Sander, R., Lelieveld, J., 2006. Technical note: a new comprehensive SCAVenging submodel for global atmospheric chemistry modelling. Atmos. Chem. Phys. 6, 565–574. https://doi.org/10.5194/acp-6-565-2006.
Usoskin, I.G., 2017. A history of solar activity over millennia. Living Rev. Sol. Phys. 14 (1), 3. https://doi.org/10.1007/s41116-017-0006-9.
Virtanen, P., Gommers, R., Oliphant, T.E., Haberland, M., Reddy, T., Cournapeau, D., et al., 2020. SciPy 1.0: fundamental algorithms for scientific computing in Python. Nat. Methods 17 (3), 261–272.
Yamagata, T., Nagai, H., Matsuzaki, H., Narasaki, Y., 2019. Decadal variations of atmospheric 7Be and 10Be concentrations between 1998 and 2014 in Japan. Nucl. Instrum. Methods Phys. Res. Sect. B Beam Interact. Mater. Atoms 455, 265–270. https://doi.org/10.1016/j.nimb.2018.12.029.
Yasunari, T., 1985. Zonally propagating modes of the global east-west circulation associated with the Southern Oscillation. Journal of the Meteorological Society of Japan. Ser. II 63 (6), 1013–1029. https://doi.org/10.2151/jmsj1965.63.6_1013.